Sustainable Plasma-Catalytic Nitrogen Fixation with Pyramid Shaped μ-Electrode DBD and Titanium Dioxide

ChemistrySelect

Research Article
doi.org/10.1002/slct.202401076

Chemistry Europe
European Chemical Societies Publishing

www.chemistryselect.org

Sustainable Plasma-Catalytic Nitrogen Fixation with Pyramid Shaped μ-Electrode DBD and Titanium Dioxide

Pradeep Lamichhane,[a] Nima Pourali,[a] Evgeny V. Rebrov,[a, b] and Volker Hessel*[a, c]

This research explores the potential of electric field enforcement in dielectric barrier discharge using specially designed pyramid-shaped μ-electrodes for a plasma-assisted nitrogen fixation process. The obtained results are compared under varying conditions, including the presence and absence of titanium dioxide (TiO_2), different oxygen concentrations in the nitrogen-feeding gas, and residence time. The results demonstrate that the μ-electrodes lead to an enhancement of nitrogen oxidation, which is further intensified by TiO_2. The introduction of 60–70% oxygen with nitrogen achieves the highest level of NO_X production. The synergistic effect of plasma and the catalytic effect of TiO_2 increase the rate of NO_X production by 20%, resulting in a 23% increase in energy yield. The introduction of TiO_2 leads to a sharp increase in NO_X production even at lower oxygen concentrations. The crucial role played by ultraviolet light-induced electron-hole pairs in TiO_2 is highlighted to promote nitrogen oxidation. Nevertheless, it is crucial to emphasize that prolonged residence times may cause the photocatalytic effect to generate alternative byproducts rather than NO_X, consequence of excessive oxidation that could prove counterproductive. These findings emphasize the potential of plasma-assisted nitrogen fixation technology in reducing energy costs and meeting the growing demand for sustainable nitrogen-based fertilizers.

Introduction

Nitrogen fixation is a redox transformation of nitrogen molecules into various nitrogen derivatives, including nitric oxide (NO), nitrogen dioxide (NO_2), ammonia (NH_3), and so on.[1] Nitrogen fixation plays a crucial role for plants since it is essential for the biosynthesis of proteins and nucleic acids. Despite the abundant nitrogen in our atmosphere, plants cannot directly absorb it from the air, and natural nitrogen fixation is inadequate to meet their demands. Consequently, researchers are investigating artificial methods of nitrogen fixation.[2] The initiation of industrial nitrogen fixation can be traced back to the Birkeland Eyde process, which emerged in 1903 AD. This process employed an electric arc to convert atmospheric nitrogen into nitric acid.[3,4] The compromised viability of this method was attributed to both the scarcity of renewable energy sources at that time and its high energy cost, which ranged from 300 to 500 GJ/t-nitrogen.[2]

In 1913 AD, two Nobel laureates, the German scientist and businessman Fritz Haber and Carl Bosch, introduced another practical alternative for nitrogen fixation on an industrial scale, commonly known as the Haber–Bosch (H–B) process.[5] In this process, nitrogen and hydrogen react over an iron-based catalyst at extreme physical conditions (400–500 °C and 150–300 atm).[5] Currently, the H–B process accounts for approximately 29% of global nitrogen fixation, yielding around 140 million tons of ammonia annually. The energy cost of this process ranges from 18 to 100 GJ/t-nitrogen.[2] Annually, 200 million tons of carbon dioxide, accounting for 75% of total greenhouse gas emissions on Earth, is utilized to generate a staggering 140 billion tons of ammonia.[5,6] Despite a century of development, approximately 60% of the global population still lacks access to these products due to the substantial energy and capital investments required for establishment and production.[7] To address this limitation of centralized production units, researchers are actively exploring alternative, sustainable small-scale production plants capable of on-site, localized nitrogen fixation on demand.

Atmospheric pressure plasma generated could be a viable alternative to the existing nitrogen fixation for the following reasons: (i) It operates under normal atmospheric conditions.[8] (ii) It uses sustainable energy sources.[9] (iii) Unlike the H–B process, it does not release any greenhouse gases into the environment.[10] (iv) The energy cost of plasma-assisted nitrogen fixation is theoretically estimated to be the lowest among contemporary technologies, ranging from 3 to 6 GJ/t-nitrogen.[2] (v) It is cost-effective in terms of establishment, production, transportation, and storage. (vi) Localized production on-site and on-demand is feasible, which means it can be conveniently used directly on farmland when needed.[11]

Besides plasma technology, some other alternative green methods for nitrogen fixation have also been proposed. Electro-

[a] P. Lamichhane, N. Pourali, E. V. Rebrov, V. Hessel
School of engineering, University of Warwick,
Coventry, West Midland, CV4 7AL, United Kingdom

[b] E. V. Rebrov
Department of Chemical Engineering and Chemistry,
Eindhoven University of Technology,
Eindhoven, 5600MB, Netherlands

[c] V. Hessel
School of Chemical Engineering, University of Adelaide,
Adelaide, 5005, Australia
E-mail: volker.hessel@adelaide.edu.au

catalysis represents one such environmentally friendly approach to nitrogen fixation. The energy cost of electrolysis can be as high as 100 GJ/t-nitrogen.[12] The primary advantage of electrocatalysis lies in its ability to modulate reaction activity and selectivity by adjusting applied potentials, which obviates the need for catalyst heating. However, the efficacy of electrocatalysis is hindered by the poor electrical conductivity of catalysts and low Faradaic efficiency, preventing the realization of desired outcomes.[13] Furthermore, photocatalysis has emerged as a promising green technology for nitrogen fixation, owing to its cost-effectiveness and minimal secondary pollution. In initial research stages, the energy cost of photocatalysis can reach up to 300 GJ/t-nitrogen.[14] Nevertheless, this method is constrained by low production efficiency and time-consuming processes.[15] Researchers have also explored the utilization of microbes for artificial nitrogen fixation, with this biological approach boasting a minimal energy cost of 16 GJ/t-nitrogen.[2] Despite being highly reactive, cost-effective, environmentally friendly, selectivity, commercial utilization is hindered by challenges such as a lack of designability, stability, insufficient availability of ready-to-use biocatalysts, and biocatalyst inactivation at high temperatures and extreme pH conditions.[16]

Atmospheric pressure plasma generated from the dielectric barrier discharge (DBD) has shown exciting results in nitrogen redox transformations.[17–22] Accelerated electrons and ions in plasma collide with nitrogen molecules. This energy impact collision either ionizes or excites the nitrogen molecules. This ionized or excited nitrogen immediately either oxidizes into *NO*, NO_2, or reduces into NH_3. DBD plasma, both with and without a catalyst, has been utilized for nitrogen oxidation in previous studies; however, the results obtained so far have fallen short of the theoretical value.[2] Pei et al.[23] employed surface DBD and achieved an energy cost of 1108 GJ/t-nitrogen. On the other hand, Liu et al.[24] utilized noncatalytic DBD plasma for nitric acid synthesis, but the energy cost remained relatively high at 619 GJ/t-nitrogen. To enhance the energy cost, Patil et al.[25] employed a Al_2O_3 catalyst-packed DBD reactor, which yielded an improved energy cost of 391 GJ/t-nitrogen. Similarly, Ma et al.[26] used a $BaTiO_2$ catalyst, further enhancing the energy cost to 347 GJ/t-nitrogen. Although there have been advancements in the field, the energy cost of nitrogen fixation using DBD plasma is still higher compared to existing technologies.

The shape of the electrode used in the plasma source plays a crucial role in determining how the plasma behaves and its characteristics. Previous studies have explored different electrode shapes such as pyramid-shaped spikes, spiral electrodes, double hexagons, and conical electrodes.[27–32] However, these studies primarily focused on the shape of the electrodes rather than their sharpness. It is assumed that such a micro-level sharpness on the end of the electrode acts as a charge emitter, which can promote a higher rate of secondary electron emission and field emission due to the intensified local electric field.[33] Furthermore, using μ-electrode DBD has proven advantageous due to its efficient output of results.[34] Nevertheless, manufacturing electrodes with exceptionally sharp tips is a challenging and costly endeavor. Therefore, when designing the structure, we have strived to achieve the highest degree of sharpness while maintaining cost-effectiveness.

There is a series of literature that has investigated the effect of oxygen concentration on plasma-assisted nitrogen fixation, encompassing a wide range of oxygen concentrations.[23,35–39] To draw comprehensive conclusions and determine whether micro discharge on DBD plasma exhibits similar behavior to microwave plasma, gliding arc, spark, corona plasma, and conventional DBD, a thorough examination involving a wide range of oxygen concentrations is necessary. Furthermore, we also aim to explore the feasibility of plasma-assisted nitrogen fixation using such specialized pyramid-shaped electrodes in combination with titanium dioxide (TiO_2) at various residence times.

The synergistic combination of photocatalyst and DBD has gained traction in recent years due to its potential for boosting product yields and energy efficiency in various processes.[40–43] This combination also opens up new possibilities for nitrogen fixation. By leveraging the synergistic effects of photocatalysis and plasma-induced reactive species, nitrogen molecules can be activated and converted into nitrogen oxides (NO_X). In this method, TiO_2 is employed to initiate photocatalytic reactions in the presence of plasma. The plasma provides the necessary energy to activate the TiO_2, while the TiO_2 catalyzes the reactions that convert N_2 into NO_X. TiO_2 proves to be a suitable photocatalyst in this context due to its stability, affordability, and excellent photocatalytic efficiency. On the other hand, nitrogen plasma produces multiple emission peaks in the range of 300 to 450 nm,[7] which is sufficient to activate the TiO_2 without relying on external energy sources.

In this research paper, we present a novel approach aimed at enhancing the nitrogen oxidation process by utilizing micrometer-thick electrodes. Our innovation lies in the use of such ultra-thin electrodes to boost secondary emission and field emission effects, a technique scarcely explored in previous reports. These electrodes exhibit remarkable potential to intensify the nitrogen oxidation process, contributing to a significant advancement in this field. Furthermore, we delve into the catalytic effect of micro discharges in conjunction with TiO_2. Our investigation encompasses a comprehensive examination of this catalytic effect, shedding plasma light on its potential applications and implications. To gain a comprehensive understanding of these effects, we meticulously monitor their behavior across a spectrum of oxygen concentrations. By doing so, we not only explore the novel application of micrometer-thick electrodes but also contribute valuable insights into the intricate interplay between nitrogen oxidation and catalysis, offering a fresh perspective on the possibilities for future research and technological advancements.

Experimental Setup and Methodology

To demonstrate the phenomenon of charge injection, a titanium coin was created, featuring 160 regular pyramids arranged in a periodic pattern as shown in Figure 1(a). Since perfectly sharp points do not exist in reality, a cone tip with a curvature radius of 25 μm was employed. These reactors are designed at the University of Adelaide in collaboration with ANFF-SA, University of South

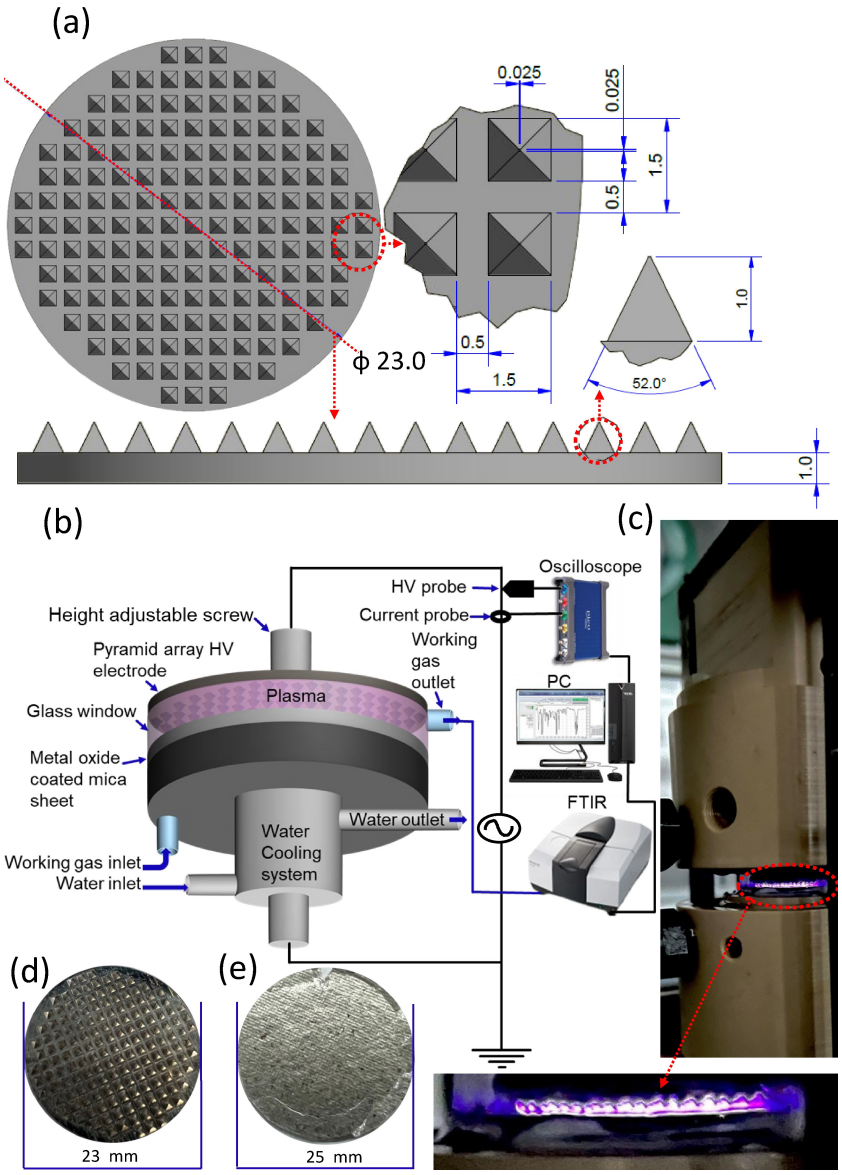

Figure 1. Schematic of (a) pyramid array electrode. Vertical and horizontal view of pyramids and their dimensions. (b) Schematic of experimental setup. Photograph of the (b) plasma reactor, (c) pyramid engraved HV electrode, and (d) TiO_2 coated mica sheet for the dielectric barrier.

Australia. The backside of the pyramids was connected to the 6 kV peak-to-peak (V_{pp}) high voltage (HV) power source. On the other hand, the ground electrode, with a diameter of 25 cm, was circular and covered by 200 μm thick dielectric layer composed of a mica sheet, with or without TiO_2 coating. To prevent arcing at the edge of the HV electrode, the circular disc of the ground electrode covered by the dielectric layer was made wider than the HV electrode. The HV disc had a diameter of 23 cm. Both electrodes were enclosed in a cylindrical quartz window with a sealed peripheral region.

To examine the influence of oxygen concentration on plasma discharge chemistry, the experiments were performed in nine different scenarios. The oxygen and nitrogen flow rates were varied while keeping the total flow rate constant at 140 sccm. By dividing the oxygen flow rate by the total flow rate of 140 sccm, the concentration of oxygen in the feeding gas was established. A Bronkhorst mass flow controller was used to regulate the gas flow. The distance between the high-voltage (HV) electrode and the ground electrode was maintained at 0.5 mm with the help of an adjustable screw. A 10 nF capacitor was utilized to measure the electric charges produced by the plasma, while a Redline Technologies G2000 served as a high-voltage power generator, generating sinusoidal waves at a fixed frequency of 68 kHz. Voltage and current values were obtained using a Tektronix P6015A 1000X high-voltage probe and a Pearson 6600 current transformer, respectively. These measurements were recorded using a pico-tec oscilloscope. The average energy dissipation was determined by calculating the area of the Lissajous figure obtained from plotting the voltage and current signals on a two-dimensional graph.

A FERGIE fiber optic spectrometer from Princeton Instruments was utilized to record the optical emission spectroscopy (OES). Vibrational temperatures were estimated with the help of OES in LIFBASE spectroscopic simulation software,[44] and the rotational temperature was estimated with the Boltzmann plot.[45] The NO_X (NO, NO_2) was detected with Fourier transform infrared spectroscopy (FTIR) from a SHIMADZU IRTracer-100 instrument. The gas from the

plasma reactor is passed into the 10 cm long continuous flow cell through the temperature-controlled thermogravimetric. The flow cell is kept inside the FTIR and the temperature is controlled at 293 K. For quantitative measurement of NO_X, the FTIR is calibrated as explained by Pei el al.[23] The synthesis rate of gas phase NO_X in grams per hour (g/hour) was calculated by multiplying the concentration of NO_X in grams per liter (g/L) with the flow rate in liters per hour (L/hour) to obtain the production rate with respect to time.

The amount of NO_X produced in grams from kilowatt-hour (kWh) energy (energy yield in g/kWh) is calculated by using Eq. (1). The reciprocal of the energy yield is energy cost in kilowatt-hours per gram (kWh/g). To express the energy cost in Joules per gram (J/g), the reciprocal of the energy yield is multiplied by 3.6×10^6 (1 kWh = 3.6×10^6 J). For industrial scale estimation, energy cost is further multiplied by 10^{-3} which converts into Giga Joules per ton of NO_X (GJ/t-nitrogen). Also, residence time refers to the average amount of time that a substance or material stays inside a specific system or reactor. It is important to understand residence time to optimize process conditions, design reactors, and scale up chemical processes. By adjusting the residence time, we can control the rate of reaction, the amount of conversion, and the selection of desired products. Residence time is usually calculated by using Eq. (2).

$$E_{yield} = \frac{NO_X \text{ synthesis rate (g/hour)}}{\text{Power (kW)}} \quad (1)$$

$$\text{Residence time} = \frac{\text{Volume of reactor}}{\text{Volumetric flow rate}} \quad (2)$$

TiO_2 is a versatile material that is widely used for photocatalysis. To improve its functionality and performance, TiO_2 was coated on a mica film using the sol-gel method. The sol-gel was synthesized by adding 43 µL of 70% w/v nitric acid to 8778 µL of ethanol in a stirring flask. This was followed by adding 1112 ml of 97% w/v titanium iso-propoxide [$TiOCH(CH_3)_24$] dropwise along with 64 µL of deionized water. The final composition of the sol-gel was $1Ti[OCH(CH_3)_2]_4:40EtOH:1.3H_2O:0.13H_2O:0.13HNO_3$. The mixture was aged under stirring for 25 hours in a sealed flask, which resulted in the formation of a clear and stable sol-gel. To prepare the mica substrate for coating, it was cleaned thoroughly using a solvent such as ethanol and allowed to dry. The humidity of the spin coater was maintained at 80%, and 200 µL of the sol-gel was coated onto the mica substrate at 1500 rpm for 30 seconds. The coating process was repeated ten times to build up the desired thickness of the TiO_2 coating. The coated substrate was then kept at room temperature to allow the solvent to evaporate. After drying, the coated substrate was calcinated for 4 hours at 400 °C with a heating rate of 1 K/min to allow the TiO_2 to crystallize and form a stable coating. However, Most of the photocatalytic nitrogen oxidation takes place within the surface of the UV-exposed TiO_2.[46,47] This process is repeated five times to achieve the necessary thickness because an extremely thin film is prone to damage due to plasma etching. The resulting TiO_2-coated mica substrate was analyzed using X-ray diffraction spectroscopy (XRD), as shown in Figure 2. The XRD pattern of the TiO_2 coated mica sheet is compared with XRD patterns of the standard anatase-TiO_2[48] and rutile-TiO_2.[49] Our results reveal that the TiO_2 is successfully coated on the mica sheet. Additionally, the water cooling system employed on the ground electrode serves to minimize the thermal effect of the plasma during the photocatalytic process.

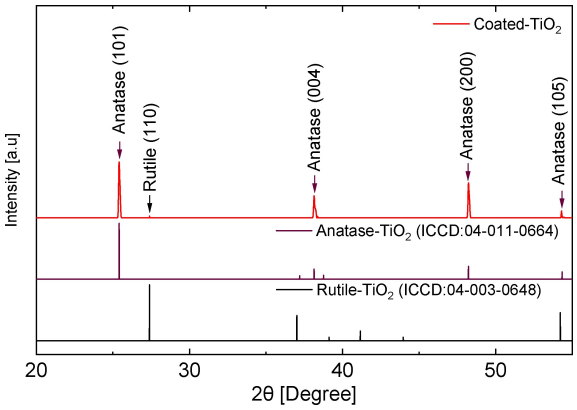

Figure 2. Comparison of XRD patterns of TiO_2 coated over the mica sheet, which is used as a dielectric barrier, with standard anatase and rutile TiO_2.

Results and Discussions

Electrical Properties

The current-voltage waveforms of a typical AC-driven plasma source with and without TiO_2 at 0%, 50%, and 100% oxygen concentration in the feeding gas are presented in Figure 3(a–c), respectively. In all cases, both the positive and negative half-cycles of the applied voltage exhibit multiple current peaks. During the positive half-cycle of the voltage waveform, the

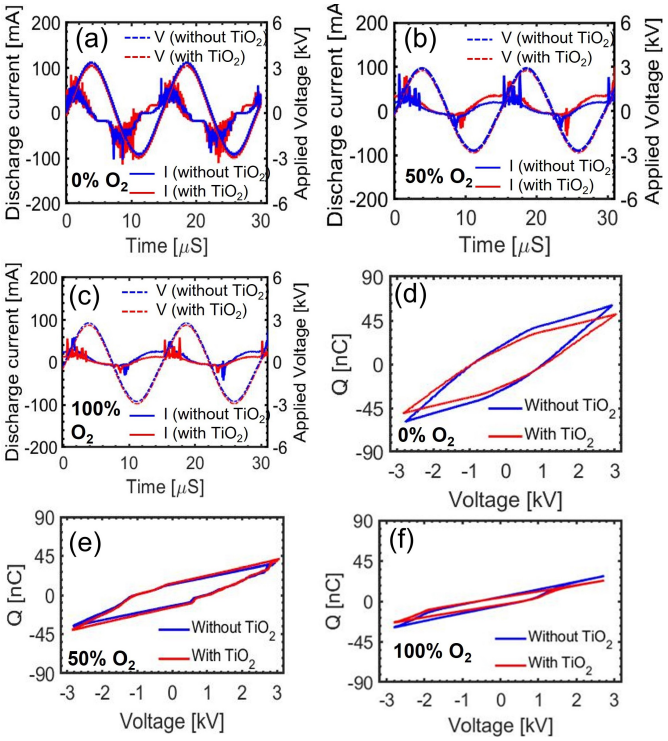

Figure 3. Variation of current-voltage waveforms with and without TiO_2 at (a) 0%, (b) 50%, and (c) 100% of oxygen mixed with nitrogen in the feeding gas. Corresponding Lissajous figures are presented in (d–f), respectively. [Applied voltage (V_{pp}) = 6 kV, frequency = 68 kHz, gap distance = 0.5 mm, gas flow rate = 140 sccm].

positive potential attracts electrons toward the positively charged electrode. As the electrons gain kinetic energy, they collide with neutral gas atoms or molecules, ionizing them and creating plasma. The positively charged ions in the plasma are accelerated toward the negatively charged electrode. Similarly, during the negative half-cycle of the voltage waveform, the opposite occurs. The negative potential attracts electrons toward the negatively charged electrode, while the positively charged ions are repelled. This leads to a reversal in the direction of electron and ion movement. This is a recurring process, and it takes approximately 14.7 μs for one complete cycle. This oscillation process increases successive collisions between electrons, neutrals, and ions. From the current-voltage waveform, it is observed that the presence of TiO_2 has no significant difference in electrical discharge but with an increase in oxygen concentration, the discharge current is significantly reduced.

The corresponding Lissajous figures of current-voltage waveform presented in Figure 3(a–c), are shown in Figure 3(d–f), respectively. Accumulated wall charge ($Q = \int_0^T I_m dt$) during the positive part of applied voltage decreases during the negative part of applied voltage[7,11] thus the net transfer of charge in a complete cycle is zero. Consequently, the voltage versus charge plot (Lissajous figure) forms a closed loop.[4,50] Measuring the area enclosed by a Lissajous loop is a common technique to determine the energy consumed by DBD in a cycle. Thus, the power (P) consumed by the plasma is given by the mathematical product of the area enclosed by a Lissajous loop and the frequency, as shown in Eq. (3).[50] In Figure 3(b), the area of the Lissajous loop decreases with an increase in oxygen concentrations at the constant applied voltage. This decreased area is attributed to the observed reduction in discharge current, as depicted in Figure 3(a–c). Where T in the equation is for the time period (1/Frequency), I_p is for plasma current, V_p is for voltages across the plasma gap, I_m is the monitoring current across in the current transformer and V_s the total applied voltage. The calculations and further information can be found in the study conducted by Pourali et al.[51]

$$P = \frac{1}{T}\int_0^T I_p V_p dt = \frac{1}{T}\int_0^T I_m V_s dt = \frac{1}{T}\int_0^T V_s dQ = \text{Frequency} \times \text{Area of lissajous Figure} \quad (3)$$

The correlation between the average energy dissipation (power) and the peak discharge current in this experiment is shown in Figure 4, considering the presence and absence of TiO_2 at various concentrations of oxygen in the feeding gas. The findings indicate that both the mean energy dissipation and the peak discharge current exhibit a decreasing trend as the oxygen concentration increases. This behavior can be attributed to the disparity in electronegativity between nitrogen and oxygen, with oxygen possessing a higher electronegativity of 3.44 compared to 3.04 of nitrogen.[52] With a higher oxygen concentration, a reduction in primary ionization is anticipated, resulting in a decline in the peak discharge current. This decrease can be elucidated by considering the electron affinity

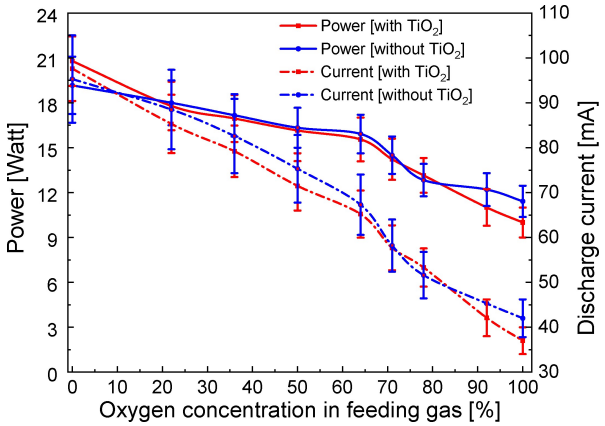

Figure 4. Variations in power and peak discharge current under various oxygen concentrations in the main flow. [Applied voltage (V_{pp}) = 6 kV, frequency = 68 kHz, gap distance = 0.5 mm, gas flow rate = 140 sccm].

of oxygen.[53] Consequently, the reduction in primary ionization leads to a decrease in the mean dissipation energy. The introduction of a TiO_2 layer on the dielectric material exhibits two simultaneous effects on plasma power. Firstly, it augments the electrical resistance of plasma, resulting in power reduction. Secondly, it serves as a catalyst, promoting plasma reactions and thereby increasing power. Considering the combined effect, the overall impact on the electrical parameters due to the addition of TiO_2 is determined to be insignificantly small.

Optical Properties

The OES of pyramid-shaped μ-electrode DBD, both with and without TiO_2 at 64% oxygen in the nitrogen main flow, is presented in Figure 5(a). The wide range of OES reveals the presence of a variety of reactive oxygen and nitrogen species. Specifically, the emission profile within the wavelength range of 311 nm to 380 nm is predominantly composed of the N_2 second positive system (SPS), corresponding to the transition $N_2(C^3\Pi_g\text{-}B^3\Pi_g)$.[53] Emission originating from the N_2 first negative system (FNS), corresponding to the transition $N_2^+(B^2\Sigma_u^+ - X^2\Sigma_u^+)$,[54] is also observed around 400 nm. Strong emission peaks from the N_2 first positive system (FPS), corresponding to the transition $N_2^+(B^3\Pi_g - A^3\Sigma_u)$,[55–57] are observed within the range of 650 nm to 850 nm. Additionally, weak emission from atomic nitrogen is observed at 741 nm, 822 nm, and 868 nm.[58] Furthermore, aside from these nitrogen emission peaks, there are prominent emission peaks from atomic oxygen at 777.2 nm, resulting from the $3p^5P \rightarrow 3s^5S$[59,60] transition, and at 844.7 nm, originating from the $3p^3P \rightarrow 3s^3S$[59,61] transition, which are also predominantly observed in the OES.

In the majority of oxygen-containing nitrogen plasma, the OES is mainly composed of nitrogen SPS, FNS, and atomic oxygen.[56,62–64] Besides this, emissions from nitrogen FPS are also reported.[65–67] It is worth noting that the simultaneous presence of peaks originating from atomic nitrogen and oxygen

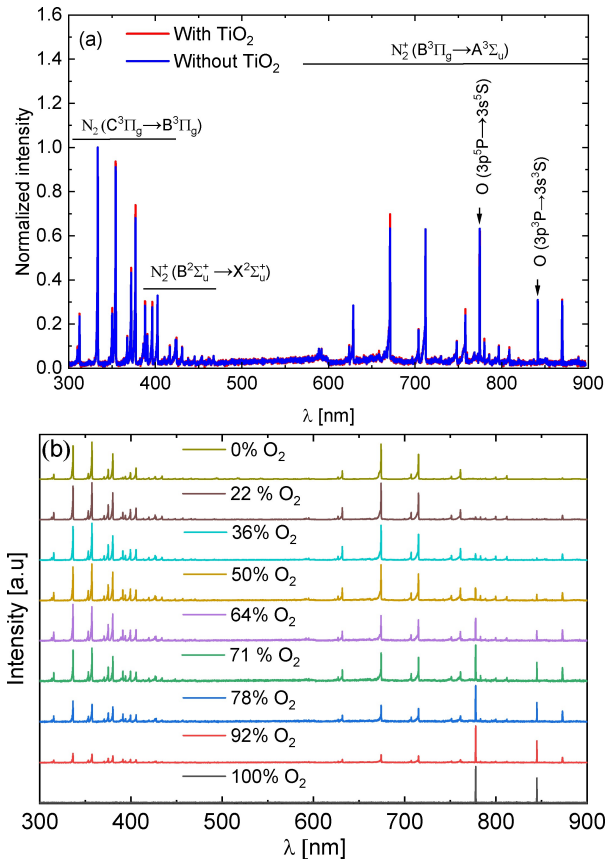

Figure 5. (a) The emission profile of various nitrogen and oxygen species with a gas mixture containing 64% oxygen in nitrogen main flow. (b) Variation of OES with various concentrations of oxygen in feeding gas [Applied voltage (V_{pp}) = 6 kV, frequency = 68 kHz, gap distance = 0.5 mm, gas flow rate = 140 sccm].

is relatively uncommon in conventional oxygen-containing nitrogen plasmas.[64,67] However, such a simultaneous appearance was also reported in a few pieces of literature on direct current glow discharge,[68] compact pulse-modulated plasma[69] and in the spark.[70] The observed distinct OES in this experiment could possibly be attributed to the enhanced electric field confined in the μ-tip of the electrode. This is likely because objects with sharper edges tend to have a higher charge density.[71] Enhancement of the electrical field and charge density in this reactor is calculated in the report of the Pourali et al.[33] The μ-tip with similar characteristics is already employed as charged injectors in field emission devices.

The optical emission profile of the plasma was captured before its interaction with a catalytic surface. Consequently, no significant differences were observed between the cases with and without the presence of TiO_2 in this experiment. As a result, the focus of the OES study shifted to exploring different concentrations of oxygen in the presence of TiO_2, as presented in Figure 5(b). Starting at 0% oxygen, the OES was found to be exclusively composed of nitrogen species. However, as the concentration of oxygen gradually increased, a fascinating transformation began to unfold. Emission peaks originating from atomic oxygen emerged and grew more pronounced with each incremental rise in oxygen concentration. This progression resulted in a remarkable decrease in the emission from nitrogen, clearly highlighting the impact of the introduced oxygen on the overall emission spectrum. When the oxygen concentration reached 100%, the OES was evidently dominated solely by the peaks of atomic oxygen.

In the context of nitrogen plasma with a sufficient quantity of oxygen, the emission spectra undergo a complete takeover by the prevalence of atomic oxygen, essentially replacing the contribution of other species. This phenomenon arises from the preferential allocation of a significant portion of electron energy towards activating molecular oxygen due to its comparatively lower. The activation energy of oxygen was found to be 26.7 kcal/mole whereas it is 38.6 kcal/mol for nitrogen.[72] The underlying cause of this behavior lies in the high electronegativity of oxygen, which promotes an efficient transfer of energy from the plasma to the oxygen molecule. As a consequence of this energy allocation preference, the availability of electron energy for activating nitrogen molecules diminishes. Consequently, the intensity of nitrogen emission experiences a reduction proportional to the increasing concentration of oxygen in the plasma. This reduction in N_2 emission intensity is a direct consequence of the augmented activation of oxygen species, leading to a distinct alteration in the emission characteristics of plasma.

Thermal Properties

The estimation of thermal plasma parameters, including the rotational temperature and vibrational temperature of nitrogen molecules, is a crucial process for understanding plasma discharge and energy transfer mechanisms. The presence or absence of TiO_2 does not significantly affect the vibrational and rotational temperatures, as evidenced by the similarities observed in the OES spectrum under both conditions. The vibrational temperature is thermal energy due vibrational motion of nitrogen molecules.[44] Vibrationally excited nitrogen molecules can easily undergo redox transformation. Vibrational temperatures are determined through the comparison of simulated spectra with experimental spectra of the N_2 FNS in the presence of TiO_2 conditions which is given in Table 1. This table also includes the rotational temperature. Estimating the rotational temperature is crucial for determining the true gas temperature or the real thermal state of the plasma. Due to the short relaxation time of nitrogen molecules, their rotational distribution quickly reaches thermodynamic equilibrium. Plasma is considered non-equilibrium or non-thermal if it exhibits a high vibrational temperature and a low rotational temperature. The ratio between the vibrational temperature and the rotational temperature holds significant importance in plasma chemistry.[44]

According to the results, as the oxygen concentrations increased from 0% to 92%, both the vibrational temperature and the rotational temperature showed an increase. When the observation points are close to each other, significant changes cannot be observed. However, if we consider a wider range,

Table 1. Variation of rotational and vibrational temperature with various concentrations of oxygen in plasma with TiO_2 [Applied voltage (V_{pp}) = 6 kV, frequency = 68 kHz, gap distance = 0.5 mm, gas flow rate = 140 sccm].

Oxygen in feeding gas [%]	T_{vib} [K]		T_{rot} [K]	
	Without TiO_2	With TiO_2	Without TiO_2	With TiO_2
0%	6217 ± 187	6233 ± 175	449 ± 12	456 ± 11
22%	6503 ± 154	6474 ± 200	459 ± 10	464 ± 13
36%	6583 ± 197	6593 ± 200	470 ± 14	472 ± 15
50%	6692 ± 200	6676 ± 203	479 ± 12	478 ± 10
64%	6713 ± 203	6764 ± 187	484 ± 17	482 ± 16
71%	6802 ± 175	6823 ± 215	485 ± 14	486 ± 12
78%	6873 ± 142	6841 ± 180	487 ± 19	490 ± 15
92%	6886 ± 162	6898 ± 112	494 ± 16	498 ± 13
100%	–	–	–	–

from 0% O_2 to 92% O_2, significant changes in both rotational and vibrational temperatures become evident. For example, at these concentrations, the vibrational temperatures are 6217 ± 187 K and 6886 ± 162 K, respectively, when oxygen concentrations increase from 0% to 92%, without the presence of a catalyst. Under the same conditions, the rotational temperatures are 449 ± 12 K and 494 ± 16 . Similar changes can be observed in the absence of TiO_2, but there is no significant difference between the results with and without the catalyst. According to the studies conducted by Joh et al.,[73] and Liu et al.,[24] both the rotational and vibrational temperatures increase as the transfer of electron energy to nitrogen molecules intensifies. As the oxygen admixture increases, the electron density is expected to decrease due to the higher electron affinity of oxygen compared to nitrogen. Oxygen molecules have a tendency to capture available free electrons. As a result, the electron density decreases, leading to an overall increase in the mean electron energy. This enhanced electron energy promotes greater energy transfer to other neutral nitrogen molecules, resulting in higher rotational and vibrational temperatures.

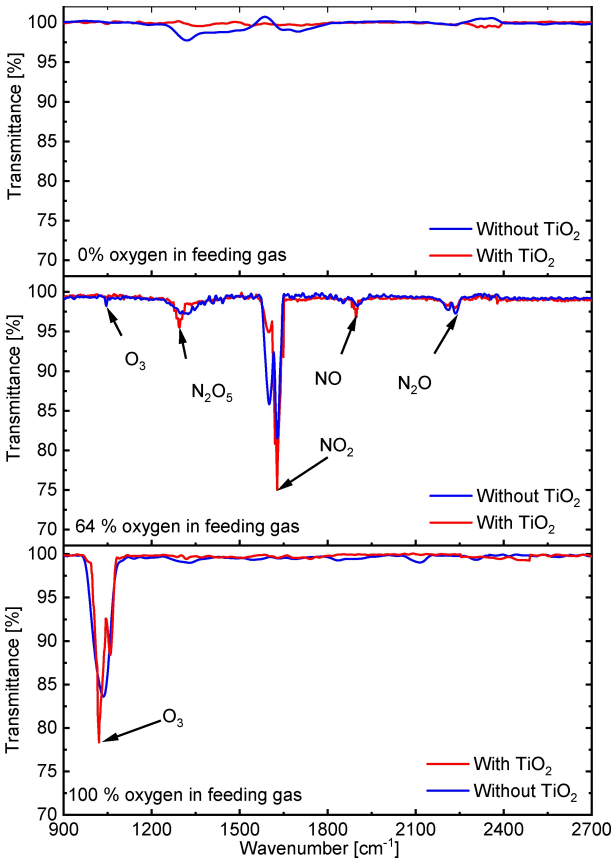

Figure 6. FTIR spectra of the plasma output gas obtained with and without TiO_2 under three different conditions: 100% oxygen (100 sccm oxygen + 0 sccm nitrogen), 64% oxygen (90 sccm oxygen + 50 sccm nitrogen), and 0% oxygen (0 sccm oxygen + 100 sccm nitrogen)[Applied voltage (V_{pp}) = 6 kV, frequency = 68 kHz, gap distance = 0.5 mm, gas flow rate = 140 sccm].

Fourier-Transform Infrared Spectroscopy

The Figure 6 illustrates representative FTIR spectra of the plasma output gas obtained with and without TiO_2 under three different conditions: 100% oxygen (100 sccm oxygen + 0 sccm nitrogen) at the bottom, 64% oxygen (90 sccm oxygen + 50 sccm nitrogen) in the middle, and 0% oxygen (0 sccm oxygen + 100 sccm nitrogen) at the top. The bottom spectrum in Figure 6 represents the FTIR of pure oxygen plasma, exhibiting distinct ozone peaks in the range of 1053–1125 cm^{-1}.[74] Interestingly, in the presence of TiO_2, the ozone peaks are more pronounced compared to their absence. As the oxygen concentration gradually increases, the ozone peaks gradually diminish, while peaks associated with NO_X begin to emerge. In the middle spectrum, multiple peaks corresponding to NO, NO_2, N_2O_5, and N_2O_5 are observed. The dominant feature in this spectrum is the NO_2 peaks within the range of 1660–1560 cm^{-1}.[75] Additionally, smaller peaks attributed to N_2O are present in 2265–2145 cm^{-1} range.[74] The strong stretch of NO_2 in N_2O_5 leads to another smaller peak around 1300–1350 cm^{-1}.[75,76] Peaks associated with NO are also visible in 1965–1770 cm^{-1} range.[75,76] Beyond this oxygen concentration,

the nitrogen oxide peaks again gradually start to decrease. Finally, the top spectrum represents the FTIR of pure nitrogen, which lacks significant peaks related to NO_X.

Figure 6 reveals that the inclusion of TiO_2 leads to enhanced nitrogen oxidation compared to conditions lacking TiO_2. The presence of TiO_2 results in elevated peaks for all nitrogen oxides; however, notably higher levels of N_2O production are observed in its absence. Intriguingly, in the presence of TiO_2, the generated N_2O undergoes rapid oxidation into NO_2; but in its absence, the NO_2 oxidation process is significantly slower. Consequently, the peaks of N_2O in the absence of TiO_2 is higher than that in its presence.

NO_X Production Rate and Energy Efficiency

During the nitrogen oxidation process, multiple products can be generated. The targeted production of nitrogen oxide can be regulated by effectively managing the nitrogen oxidation process within the confines of the reaction chamber. In this specific experiment, the quantification efforts focus solely on the measurement of NO, NO_2 species, which collectively contribute to the assessment of the total gas-phase NO_X concentration. As we aimed to see the effect of oxygen concentration in the plasma catalytic nitrogen oxidation process, various concentrations of NO, NO_2, and total NO_X in the plasma output gas with various oxygen concentrations in the presence or absence of TiO_2 is shown in Figure 7(a). In accordance with the observed FTIR spectrum, NO_X were found to be minimal in the nitrogen plasma, gradually increasing as the oxygen flow rate increased. Notably, the concentration of NO was consistently 5 to 10 times lower than the concentration of NO_2, regardless of the presence or absence of the catalyst.

The highest concentrations of NO are achieved when the oxygen concentration ranges from 40% to 50%. However, the maximum concentration of NO_X is observed at an oxygen concentration of 60% to 70%. This difference in concentration could be attributed to the excessive formation of nitrogen dioxide NO_2 in this specific region. At an oxygen concentration of 64%, the concentration of NO_2 increases from 17.1 mg/L to 20.2 mg/L when TiO_2 is present. Additionally, the concentrations of NO_X increase from 20.4 mg/L to 24.5 mg/L with the addition of TiO_2. The catalytic activity of TiO_2 is responsible for these increases, resulting in a 25% increase in NO concentration and a 19% increase in NO_2 concentration. Overall, these increases contribute to a total 20% increase in the rate of NO_X synthesis. However, beyond this oxygen concentration, the concentrations of NO_X start to decrease continuously because of the limited availability of nitrogen species at higher oxygen concentrations in the feeding gas. Eventually, as the oxygen concentration reaches 100%, the NO_X concentrations disappear entirely.

Figure 7(b) demonstrates the relationship between oxygen concentration and their effects on the energy yield and energy cost of synthesizing NO_X. As observed in Figure 4, there is no significant difference in power consumption between the cases with and without catalysis. Therefore, in this experiment, the production rate of NO_X is the sole factor affecting the energy

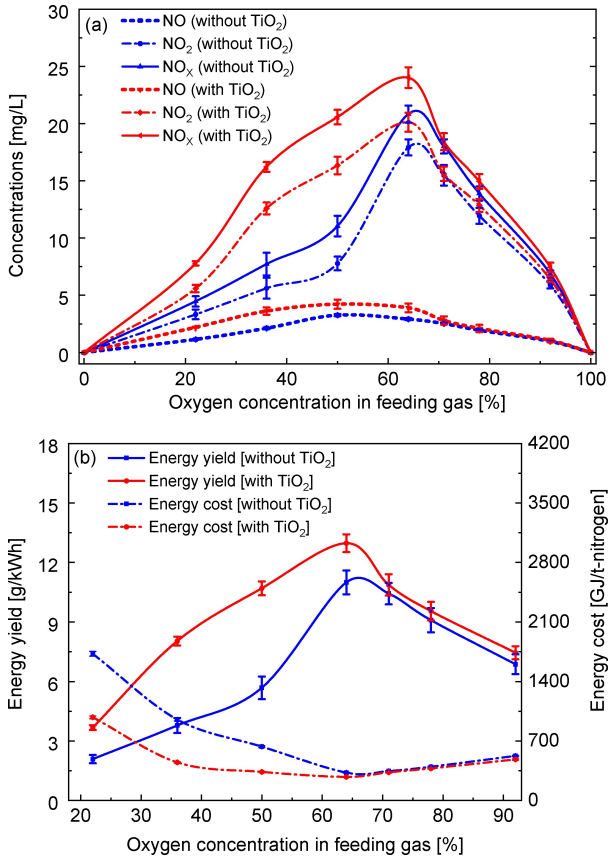

Figure 7. Variation of (a) NO_X production rate, (b) energy yield and energy cost with various oxygen concentrations in nitrogen main flow in the presence and absence of TiO_2 [Applied voltage (V_{pp}) = 6 kV, frequency = 68 kHz, gap distance = 0.5 mm, gas flow rate = 140 sccm].

yield or energy cost. With an increase in the production rate, the energy yield also increases, while the energy cost decreases significantly. The trend of energy yield is consistent with the trend of production rate, as shown in Figure 7(a). However, the trend of the energy cost is just the opposite, with higher production rates resulting in lower energy costs. Figure 7(b) excludes data points for pure oxygen plasma and pure nitrogen plasma since they did not yield significant production of NO_X. Consequently, the energy yield for these cases would be zero, while the energy cost would be indefinitely high.

At an oxygen concentration of 64% in the main feeding gas, the utilization of the TiO_2 resulted in a maximum energy yield of 13.5 g/kWh, whereas without the presence of TiO_2, the energy yield was only 10.9 g/kWh under the same operating conditions. Additionally, at this specific condition, the energy cost reached a minimum value of 266.1 GJ/t-nitrogen with TiO_2, whereas it was higher at 327.5 GJ/t-nitrogen without TiO_2. Incorporating the catalytic activity contributed to a 24% increase in energy yield. Although these results represent progress, they are still not comparable to existing technologies in terms of efficiency. As of now, the plasma-assisted nitrogen fixation process is not competitive for large-scale production plants. However, it can be applicable for small-scale localized plants, offering potential benefits in terms of avoiding certain

costs associated with establishment, production, storage, and transportation.[77,78]

To bring plasma-assisted nitrogen fixation technology from the laboratory to the farm, it is indeed crucial to estimate the energy yield or energy cost associated with its implementation. This estimation helps evaluate the feasibility and efficiency of the technology in practical agricultural settings. The energy yield refers to the amount of desired products obtained from the system compared to the energy input. It involves assessing the efficiency of the plasma-assisted nitrogen fixation process in converting the input energy into useful fixed nitrogen compounds. On the other hand, the energy cost involves evaluating the total energy consumption for a plasma-assisted nitrogen fixation system. Estimating the energy yield or energy cost typically requires conducting detailed experimental studies and analyzing the performance of the system under various conditions. The specific parameters to be considered may include plasma power consumption, reactant gas flow rates, conversion efficiencies, and overall system efficiency. By quantifying the energy yield or energy cost, researchers and stakeholders can make informed decisions regarding the scalability, economic viability, and environmental impact of implementing plasma-assisted nitrogen fixation technology on a larger scale in agricultural practices.

The Significance of The μ-Electrode in Nitrogen Fixation

The pointed tip of the pyramid electrode exhibits a small curvature, which results in a higher charge density. Consequently, this leads to a stronger electric field at the tip, where the electron density is greater.[78] This sharp tip has the potential to increase the likelihood of vibrational excitation or ionization of the surrounding gas molecules.[33] Figure 8 illustrates a schematic representation of the pyramid electrode and intensified electric field at the end of the pyramid electrode. This intensified electric field boosts velocity, ultimately increasing the rate of secondary electron emission.[33] Furthermore, it has been reported that a strong electric field can enhance both electron density and electron temperature.[33] These energies are transferred to neutral nitrogen molecules during electron impact collisions.

The process of nitrogen fixation is initiated by either the dissociation or excitation of the nitrogen molecule ($N{\equiv}N$).[80] The nitrogen triple bond is widely recognized as one of the strongest bonds due to its high dissociation energy, requiring excitation energy ranging from 1.5 to 4.0 eV ($1.4{\times}10^5{-}3.8{\times}10^5$ *J/mol*),[80] possessing a bond dissociation energy of approximately 9.1 eV ($8.7{\times}10^5$ *J/mol*),[4] and ionization energy of about 14.33 eV ($1.4{\times}10^6$ *J/mol*).[81] Consequently, a substantial amount of energy is necessary to break or excite this bond and facilitate artificial nitrogen fixation. In DBD, electron temperatures are typically on the order of a few electron volts.[82,83] These electrons possess enough energy for vibrational excitation, breaking, or exciting the molecular bonds of $N{\equiv}N$ and $O{=}O$. In the first phase, the nitrogen molecules were excited and dissociated through the process shown in Eqs. (4) and (5).[84–86]

$$N_2 + e \rightarrow N_2^*(^1\Sigma_g^+, v) + e \tag{4}$$

$$N_2^*(^1\Sigma_g^+, v) + e \rightarrow 2N + e \tag{5}$$

The sharp tips or edges on electrodes can facilitate the formation of streamers or filaments in the plasma, which are known to enhance the plasma volume and increase the residence time of reactive species. Which ultimately increases the concentration of N_2^* and N in the plasma phase.[34] In the second step, a secondary endothermic process occurs, leading to the formation of *NO* through Zeldovich reactions, as shown in Eqs. (6) and (7).[87]

$$O(^3P) + N_2^*(^1\Sigma_g^+, v) \rightarrow NO(^2\Pi) + N(^4S), \quad E_a \approx \Delta H \approx 3\ \text{eV/molecule} \tag{6}$$

$$N + O_2 \rightarrow NO + O, \quad E_a \approx 0.3\ \text{eV/molecule},\ \Delta H \approx -1\ \text{eV/molecule} \tag{7}$$

To generate *NO*, it is essential to have both nitrogen and oxygen molecules present in nearly equal proportions. The experimental results in Figure 7(a) demonstrate that the highest

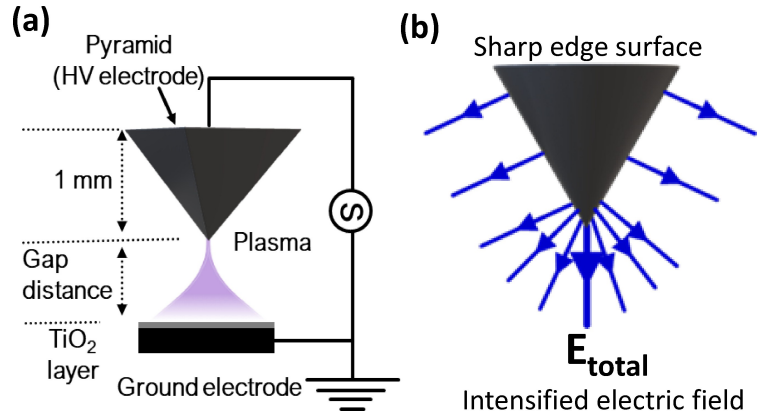

Figure 8. Schematic of (a) pyramid-shaped micro-electrode electrode and (b) Intensified electric field at the tip of the pyramid.

concentration of *NO* is produced when there is an approximately 50% mixture of O_2 with N_2. However, to achieve the highest yield of NO_X, a slightly higher proportion of O_2 than N_2 is required. This is because the lifetime of *NO* at the temperature of DBD is approximately 1.4 μs, and it is immediately oxidized into NO_2 in the presence of additional O_2,[88] as depicted in Eq. (8).[20,89–91]

$$NO + O \rightarrow NO_2,\ \alpha_{NO_2} = 2.6 \times 10^{12}\ cm^{-13}\ molec^{-1}\ s^{-1} \quad (8)$$

It has been reported that the vibrational levels of N_2 play a crucial role in facilitating the energy-efficient formation of NO_X. However, this positive impact of the N_2 vibrational levels is attenuated by collisions with the vibrational levels of O_2.[37] This phenomenon arises due to the exchange of vibrational energy between N_2 and O_2 molecules. The aforementioned report also offers an elucidation of the underlying mechanisms through a chemical kinetics model, which has been validated through experiments conducted in a gliding arc. In other sources of plasma, such as microwave plasma, gliding arc, and spark (also known as warm plasma), exhibit significantly higher gas temperatures compared to DBD plasma.[92] At these elevated temperatures, a larger amount of energy becomes available to drive the endothermic reaction responsible for the production of *NO*, as described in Eqs. (6) and (7). As a result, most of the research on the effect of oxygen concentration on plasma-assisted nitrogen fixation, including studies involving microwave plasma,[35] spark,[23,36] and gliding arc,[37] has observed peak performance at approximately 50% oxygen concentration.

The experimental findings presented in this study using DBD also reveal similar results for *NO* concentration. However, the overall concentration of *NO* is relatively small compared to that of NO_2. This discrepancy in concentrations can be attributed to the prevailing conditions in DBD plasma. At lower temperatures, such as those found in DBD plasma, there is limited energy available to drive the reaction described in Eq. (6). As a result, the majority of *NO* is formed through the reaction in Eq. (7), which is immediately further oxidized into NO_2 through the mechanism shown in Eq. (8). At low oxygen concentrations, the yield of NO_X is low because there are insufficient oxygen molecules present to react with the nitrogen molecules. In the oxygen concentration range of 60% to 70%, the NO_X yield is at its maximum in this experiment due to the favorable ratio of nitrogen to oxygen in NO_2, which falls within this range. Finally, at high oxygen concentrations, the yield of NO_X decreases because a significant portion of the energy is consumed by the excitation and dissociation of oxygen molecules. Furthermore, an increase in oxygen concentrations can also lead to a reduction in plasma discharge due to the electronegativity of the oxygen molecule.

All nitrogenous products such as NH_3 and NO_X carry equal importance for their intended applications, and they can be chemically interchanged. The energy required for producing ammonia through the capture and catalytic reduction of NO_X is estimated at 1.50 MJ per mole of NH_3.[93] However, NO_X dissolved in soil stands out as highly versatile precursors for nitrogen-based fertilizers when compared to NH_3/NH_4^+, especially due to their mobility in the soil, which facilitates more efficient plant uptake. In localized small-scale nitrogen fixation, nitrogen oxidation is easier and less complex compared to nitrogen reduction. Additionally, the utilization of NH_3 necessitates the incorporation of hydrogen, which introduces a more intricate feed-stock requirement compared to oxygen.

Role of Titanium Dioxide in Nitrogen Oxidation

Photocatalysis offers a green and sustainable approach for both the synthesis and degradation of diverse compounds by utilizing light energy to drive environmentally friendly chemical transformations.[40–43,94–97] The fundamental concept of photocatalysis involves the conversion of photon energy (*hv*) into electrical energy within an n-type semiconductor when exposed to light.[98] The band gap of TiO_2 is approximately 3.2 eV, and the minimum wavelength required to generate an electron and hole charge-carrier pair is approximately 382 nm.[7] Several emission peaks within the photo-excitation wavelength range of TiO_2 have been observed from the nitrogen-containing plasma.[56,62–64,99] Furthermore, Sharma et al.[99] reported that nitrogen-containing plasma irrigation on TiO_2 gives promising results regarding photo-catalytic activity.

Figure 9 depicts the proposed mechanism of the photocatalytic nitrogen oxidation process in TiO_2 using plasma-generated UV light. The report by Zhang et al. provides a comprehensive explanation of the oxidation of nitrogen in the valence band (VB) and the reduction of oxygen at the conduction band (CB).[100] Additionally, detailed information about the reactions in the VB and CB of the TiO_2 can be found in the supporting information of Yuan et al.[101] In brief, When

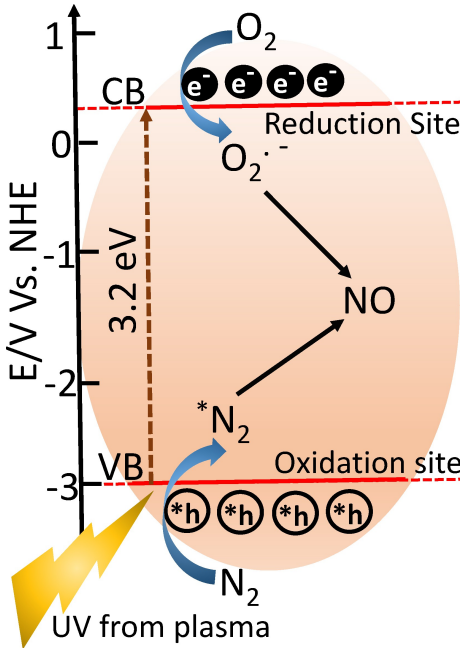

Figure 9. Schematic of the excitation of the TiO_2 photocatalyst with the help of plasma-generated UV light, and the proposed mechanism of nitrogen fixation resulting from the synergistic effect of the photocatalyst and plasma.

UV light of sufficient wavelength irradiates the surface of TiO_2, negatively charged electrons (e^-) migrate from the valence band (VB) to the conduction band (CB) of TiO_2, while positively charged holes (*h) remain in the VB,[102–104] as shown in Eqn. (9). In the CB, O_2 is reduced to superoxide (O_2^-) as presented in Eqn. (10). Simultaneously, N_2 is adsorbed on the surface of TiO_2. The electron-deficient state of the valence band facilitates the adsorption of N_2, leading to the formation of activated $*N_2$, as shown in Eqn. (11). Subsequently, the activated $*N_2$ and O_2^- species react with each other to form *NO. Finally, the *NO species desorb from the surface of the photocatalyst, yielding the NO as a product. However, it is important to note that currently, there is no experimental evidence supporting this proposed mechanism, necessitating further in-depth investigation in the future. Subsequently, NO can easily undergo further oxidation into various products such as NO_2 and N_2O_5.

$$\text{Photo excitation}: \xrightarrow{Ti_O_2} e^- +^* h \tag{9}$$

$$\text{Reduction at conduction band}: O_2 + e^- \rightarrow O_2^{\cdot -} \tag{10}$$

$$\text{Oxidation at valence band}: N_2 +^* h \rightarrow^* N_2 \tag{11}$$

Multiple studies have suggested that oxygen vacancies serve as prevalent active sites for the activation and dissociation of oxygen atoms.[100,101,105,106] These activated oxygen species play a pivotal role in nitrogen oxidation by facilitating both the chemical adsorption of N_2 and the efficient transfer of photo-excited carriers between the photocatalyst and adsorbed nitrogen molecules.[106] Operating as defects, oxygen vacancies possess electron-capturing abilities, modulate energy band structures, broaden light response ranges, and enhance the separation efficiency of photo-generated electrons and holes. Additionally, they serve as centers for surface charge separation, exposing numerous coordination unsaturated points that act as activation centers for nitrogen molecules and weaken the $N{\equiv}N$ triple bond.[106]

Drawing from literature,[100,101] the interaction between photo-generated electron-hole pairs and adsorbed oxygen molecules on the surface-active site of TiO_2 leads to the formation of O_2^- through processes such as electron transfer and hole scavenging. According to Wang et al.,[105] oxygen vacancies in metal oxides exhibit strong fluidity. This is due to the thermal activation process involving oxygen diffusion and vacancy migration, resulting in the migration of these defects from the core to the surface after heat treatment obtained from the plasma. The rearrangement of oxygen vacancies reduces the core defect of TiO_2 as a charge composite center, thereby enhancing the efficiency of charge separation and nitrogen fixation. The pursuit of photocatalytic nitrogen fixation highlights the effectiveness of enhancing surface defects.[107] Utilization of metal oxide as a photocatalysts for nitrogen fixation has shown potential improvement of ideally up to 30.9 times.[106]

The effect of TiO_2 is more pronounced under conditions of low oxygen concentration, as shown in Figure 7(a). The plasma-induced photocatalytic effect on TiO_2 becomes evident when a sufficient amount of light falls within the range of 300–400 nm (UV A) from plasma incident on the TiO_2 surface. At lower levels of oxygen concentrations in the feeding gas (higher concentration of nitrogen feeding gas), more nitrogen peaks are detected between 300–400 nm, as illustrated in the OES (Figure 5(b)). These peaks within the range of UV A serve as photon energy, essential for kickstarting the photocatalytic effect of TiO_2. However, with an increase in oxygen concentration, the nitrogen peaks decrease, subsequently reducing the availability of UV light. Consequently, this reduction leads to a notable decrease in photocatalytic activity. Although the maximum photocatalytic effect is observed at lower oxygen concentrations, NO_X synthesis is still limited due to the scarcity of oxygen. In the range of 40% to 70% oxygen concentration, an optimal combination of nitrogen, oxygen, and photons results in the maximum nitrogen oxidation. On the other hand, at higher oxygen concentrations, the intensity of UV light originating from the nitrogen second positive system diminishes significantly. As a result, there is no significant difference in NO_X production whether TiO_2 is used or not, especially above 70% oxygen concentration.

The residence time plays a critical role in nitrogen oxidation. Residence time refers to the duration that reactant species spend within the plasma environment, and it greatly influences the reaction kinetics and product distribution. By adjusting the residence time, the contact between the reactants and highly reactive plasma species can be optimized, enabling enhanced reaction rates and selectivity. Longer residence times allow for more extensive molecular collisions, providing ample opportunities for reactions to occur. Conversely, shorter residence times are advantageous for preventing excessive energy losses and minimizing unwanted side effects. Therefore, carefully controlling the residence time in plasma reactions is crucial for achieving the desired outcomes, balancing the need for prolonged exposure to plasma with considerations such as energy consumption and reactor design.

In this experiment, we investigated the impact of residence time on the rate of NO_X synthesis. To control the residence time, we adjusted the total flow rate while maintaining a constant oxygen concentration at 64%. The results are shown in Figure 10. The discharge pattern was almost uniform within the flow rate that had been changed to achieve the desired residence time used in this experiment. Additionally, the light emitted by the plasma was also uniform within this flow due to the uniform oxygen and nitrogen admixture and similar discharge phenomenon. Therefore, throughout this process, the main change in the reaction mechanism was caused by the interaction time. Interestingly, we observed that in the absence of TiO_2, the NO_X concentrations showed a slight increase as the residence time increased. Specifically, when the residence time was extended from 0.19 seconds to 0.72 seconds, the NO_X concentration increased from 19 mg/L to 22 mg/L. This suggests that the prolonged reaction time resulting from an increased residence time may be responsible for the higher NO_X production.

However, in the presence of TiO_2, the trend of variation in NO_X concentration with respect to residence time is the

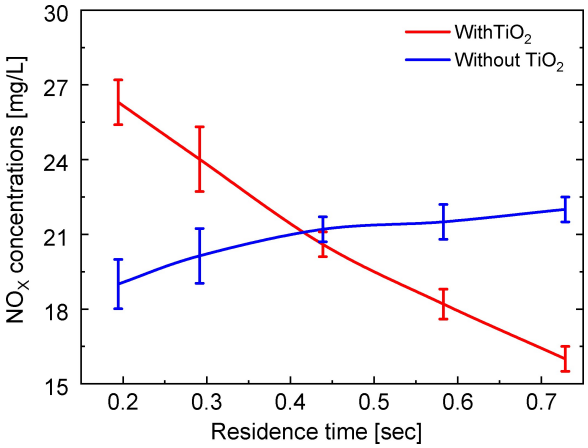

Figure 10. The effect of residence time on the NO_X synthesis rate [Applied voltage (V_{pp}) = 6 kV, frequency = 68 kHz, gap distance = 0.5 mm, gas flow rate = 140 sccm].

opposite. The concentration of NO_X decreases significantly as the residence time is increased. This behavior is illustrated in Figure 10, where an increase in residence time from 0.19 seconds to 0.72 seconds results in a decrease in NO_X concentration with TiO_2 from 26 mg/L to 16 mg/L. These findings suggest that in this context, TiO_2 may not have a dual role but instead enhances the oxidation process to form nitrogen derivatives other than NO_X. In shorter residence times, TiO_2 acts as a catalyst, facilitating oxidation. However, in longer residence times, TiO_2 exhibits a detrimental effect on NO_X. In shorter residence times, nitrogen is primarily oxidized to NO or NO_2. However, with longer residence times, nitrogen undergoes further oxidation, leading to the formation of N_2O_5 and other byproducts. In summary, as the residence time increases, TiO_2 promotes the oxidation of nitrogen. However, excessive oxidation results in the formation of undesired byproducts. A study conducted by Capp et al.[94] provides further insights into this phenomenon.

The stability of the catalyst is a crucial aspect that demands careful consideration. Elevated temperatures, the presence of reactive species, and electronic or ionic etching during plasma treatment can potentially cause surface modifications. Evaluating the stability of the catalyst under these conditions is imperative to ensure its long-term performance and practical viability beyond the laboratory setting. To address these concerns, we implemented a water cooling system to minimize thermal damage, and the catalyst was replaced every 3 hours of operation. This replacement interval also afforded the electrode a respite from elevated temperatures. Notably, the electrode is crafted from titanium, featuring a pyramid-shaped tip known for its comparative durability. Nonetheless, the longevity of the electrode is contingent upon factors such as temperature and the composition of the feeding gas. Future research should primarily focus on investigating both the cyclicity and stability of the catalyst in the context of plasma-assisted catalytic nitrogen fixation. This investigation can be conducted using comprehensive characterization techniques, including surface analysis, structural studies, and performance evaluation over extended periods. Gaining a deep understanding of cyclicity and stability will not only contribute to the fundamental comprehension of the catalytic process but also facilitate the development of more efficient and durable plasma-assisted catalytic systems for practical implementation. Such advancements hold promise for the successful application of plasma-assisted nitrogen fixation in real-world scenarios, ultimately contributing to sustainable and energy-efficient nitrogen-based processes.

Conclusions

This research paper aims to employ a fast-modulated μ-electrode dielectric barrier discharge for plasma catalytic nitrogen oxidation. The unique geometry of the pyramid-shaped μ-tips of the high-voltage electrode is leveraged to enhance nitrogen oxidation. The effects of these electrodes are observed at different oxygen concentrations, both with and without titanium dioxide, and at various residence times. Optimal NO_X production requires 60% to 70% oxygen in nitrogen. After the incorporation of titanium dioxide, a 20% increase in NO_X production and a 23% improvement in energy yield were achieved. Ultraviolet light-induced electron-hole pairs in titanium oxide particles play a crucial role in facilitating the generation of reactive nitrogen species, which can subsequently be oxidized into NO_X. However, it is essential to note that at longer residence times, the catalytic effect may generate alternative byproducts instead of NO_X due to excessive oxidation. This aspect should be considered carefully as it may yield counterproductive outcomes. These findings provide valuable insights for advancing plasma-assisted nitrogen fixation technologies and present potential avenues for optimizing nitrogen oxidation efficiency. Further research is warranted to delve into the underlying mechanisms and optimize the photocatalytic process to mitigate the formation of unwanted byproducts. Such research endeavors will contribute to the progress of sustainable nitrogen fixation methods, crucial for addressing global energy and environmental challenges.

Ethical Approval

This experiment does not involve the use of any humans or animals.

Author Contributions

Pradeep Lamichhane: Conceptualization, investigation, software, writing the original draft, review, and editing. **Nima Pourali**: Investigation. **Evgeny V. Rebrov**: Writing, review, editing, and resources. **Volker Hessel**: Conceptualization, writing, review, editing, supervision, resources, project administration, funding acquisition.

Acknowledgements

This work is supported by the ERC Synergy Grant "Surface-COnfined Fast Modulated Plasma for Process and Energy Intensification" (SCOPE), from the European Commission, with Grant No. 810182. We are particularly grateful for the assistance of Joe Gregory and Katie S. Pickering from the Department of Chemistry, University of Warwick, for XRD measurements.

Conflict of Interests

The authors state that they have no conflicts of interest to disclose in this situation. We declare that the authors have no competing interests or other interests that might be perceived to influence the results reported in this paper.

Data Availability Statement

The data that support the findings of this study are available from the submitting author upon reasonable request.

Keywords: nitrogen fixation · micro-discharge · pyramid electrode · energy yield · energy cost

[1] K. Fisher, W. E. Newton, et al., *Nitrogen fixation at the millennium*. Amsterdam: Elsevier **2002**, pages 1–34.
[2] N. Cherkasov, A. Ibhadon, P. Fitzpatrick, *Chem. Eng. Process.* **2015**, *90*, 24.
[3] H. S. Eyde, *J. R. Soc. Arts* **1909**, *57*, 568.
[4] P. Lamichhane, R. Paneru, L. N. Nguyen, J. S. Lim, P. Bhartiya, B. C. Adhikari, S. Mumtaz, E. H. Choi, *React. Chem. Eng.* **2020**, *5*, 2053.
[5] P. Peng, P. Chen, C. Schiappacasse, N. Zhou, E. Anderson, D. Chen, J. Liu, Y. Cheng, R. Hatzenbeller, M. Addy, et al., *J. Cleaner Prod.* **2018**, *177*, 597.
[6] L. Lin, H. Xu, H. Gao, X. Zhu, V. Hessel, *J. Phys. D* **2020**, *53*, 133001.
[7] P. Lamichhane, B. C. Adhikari, L. N. Nguyen, R. Paneru, B. Ghimire, S. Mumtaz, J. S. Lim, Y. J. Hong, E. H. Choi, *Plasma Sources Sci. Technol.* **2020**, *29*, 045026.
[8] V. Hessel, M. Escribà-Gelonch, M. K. Sojitra, R. Pranggono, D. Kinasz, C. Zhuang, K. Davey, M. McLaughlin, N. N. Tran, *Green Chem.* **2023**, *25*, 755–770.
[9] V. Hessel, A. Anastasopoulou, Q. Wang, G. Kolb, J. Lang, *Catal. Today* **2013**, *211*, 9.
[10] I. Muzammil, D. H. Lee, D. K. Dinh, H. Kang, S. A. Roh, Y.-N. Kim, S. Choi, C. Jung, Y.-H. Song, *RSC Adv.* **2021**, *11*, 12729.
[11] P. Lamichhane, M. Veerana, J. S. Lim, S. Mumtaz, B. Shrestha, N. K. Kaushik, G. Park, E. H. Choi, *Int. J. Mol. Sci.* **2021**, *22*, 5360.
[12] K. H. Rouwenhorst, Y. Engelmann, K. van't Veer, R. S. Postma, A. Bogaerts, L. Lefferts, *Green Chem.* **2020**, *22*, 6258.
[13] N. Yuan, Q. Jiang, J. Li, J. Tang, *Arab. J. Chem.* **2020**, *13*, 4294.
[14] Y. Sun, Y. Ahmadi, K.-H. Kim, J. Lee, *Renewable Sustainable Energy Rev.* **2022**, *170*, 112967.
[15] W. Jiang, J. Low, K. Mao, D. Duan, S. Chen, W. Liu, C.-W. Pao, J. Ma, S. Sang, C. Shu, et al., *J. Am. Chem. Soc.* **2020**, *143*, 269.
[16] C. Taylor, R. Noceti, *Catal. Today* **2000**, *55*, 259.
[17] B. S. Patil, A. S. Van Kaathoven, F. J. Peeters, N. Cherkasov, J. Lang, Q. Wang, V. Hessel, *J. Phys. D* **2020**, *53*, 144003.
[18] Y. Miao, A. Yokochi, G. Jovanovic, S. Zhang, A. von Jouanne, *Green Energy and Resources* **2023**, page 100004.
[19] W. Li, S. Zhang, J. Ding, J. Liu, Z. Wang, H. Zhang, J. Ding, L. Chen, C. Liang, *ACS Sustainable Chem. Eng.* **2023**, *11*, 1168–1177.
[20] I. Tsonev, C. O'Modhrain, A. Bogaerts, Y. Gorbanev, *ACS Sustainable Chem. Eng.* **2023**, *11*, 1888.
[21] D. K. Dinh, I. Muzammil, W. S. Kang, D. Kim, D. H. Lee, *Plasma Sources Sci. Technol.* **2021**, *30*, 055020.
[22] I. Muzammil, Y.-N. Kim, H. Kang, D. K. Dinh, S. Choi, C. Jung, Y.-H. Song, E. Kim, J. M. Kim, D. H. Lee, *ACS Energy Lett.* **2021**, *6*, 3004.
[23] X. Pei, D. Gidon, Y.-J. Yang, Z. Xiong, D. B. Graves, *Chem. Eng. J.* **2019**, *362*, 217.
[24] Z. Liu, Y. Tian, G. Niu, X. Wang, Y. Duan, *ChemSusChem* **2021**, *14*, 1507.
[25] B. Patil, N. Cherkasov, J. Lang, A. Ibhadon, V. Hessel, Q. Wang, *Appl. Catal. B* **2016**, *194*, 123.
[26] Y. Ma, Y. Wang, J. Harding, X. Tu, *Plasma Sources Sci. Technol.* **2021**, *30*, 105002.
[27] D. Amri, Z. Nawawi, M. I. Jambak, *Iop. Conf. Ser. Mater. Sci. Eng.* **2019**, *620*, 012091.
[28] B. Gilbart, A. Dickenson, J. L. Walsh, M. I. Hasan, *Plasma Processes Polym.* **2022**, *19*, 2100181.
[29] M. Takayama, K. Ebihara, H. Stryczewska, T. Ikegami, Y. Gyoutoku, K. Kubo, M. Tachibana, *Thin Solid Films* **2006**, *506*, 396.
[30] Z.-J. Liu, W.-C. Wang, D.-Z. Yang, S. Wang, S. Zhang, K. Tang, P.-C. Jiang, *Spectrochim. Acta Part A* **2014**, *121*, 698.
[31] Z.-j. Liu, W.-c. Wang, D.-z. Yang, S. Zhang, Y. Yang, K. Tang, *J. Appl. Phys.* **2013**, *113*, 233305.
[32] K. Takaki, M. Shimizu, S. Mukaigawa, T. Fujiwara, *IEEE Trans. Plasma Sci.* **2004**, *32*, 32.
[33] N. Pourali, V. Hessel, E. V. Rebrov, *Plasma Chem. Plasma Process.* **2022**, *42*, 619.
[34] P. Lamichhane, N. Pourali, E. V. Rebrov, V. Hessel, *Plasma Chemistry and Plasma Processing* **2023**, pages 1–24.
[35] O. S. Bahnamiri, C. Verheyen, R. Snyders, A. Bogaerts, N. Britun, *Plasma Sources Sci. Technol.* **2021**, *30*, 065007.
[36] K. Kučerová, Z. Machala, K. Hensel, *Plasma Chem. Plasma Process.* **2020**, *40*, 749.
[37] E. Vervloessem, M. Aghaei, F. Jardali, N. Hafezkhiabani, A. Bogaerts, *ACS Sustainable Chem. Eng.* **2020**, *8*, 9711.
[38] B. S. Patil, F. Peeters, G. J. van Rooij, J. Medrano, F. Gallucci, J. Lang, Q. Wang, V. Hessel, *AIChE J.* **2018**, *64*, 526.
[39] B. Patil, Q. Wang, V. Hessel, J. Lang, *Alternative energy sources for green chemistry* **2016**, page 296.
[40] S. Meng, A. Wang, P. He, H. Song, *J. Phys. Chem. Lett.* **2020**, *11*, 3877.
[41] W. Saoud, A. A. Assadi, M. Guiza, S. Loganathan, A. Bouzaza, W. Aboussaoud, A. Ouederni, S. Rtimi, D. Wolbert, *Appl. Catal. B* **2019**, *241*, 227.
[42] D. Mei, X. Zhu, C. Wu, B. Ashford, P. T. Williams, X. Tu, *Appl. Catal. B* **2016**, *182*, 525.
[43] V. Palma, M. Cortese, S. Renda, C. Ruocco, M. Martino, E. Meloni, *Nanomaterials* **2020**, *10*, 1596.
[44] N. C. Roy, N. Maira, C. Pattyn, A. Remy, M.-P. Delplancke, F. Reniers, *Chemical Engineering Journal* **2023**, page 141844.
[45] B. Ghimire, J. Sornsakdanuphap, Y. J. Hong, H. S. Uhm, K.-D. Weltmann, E. H. Choi, *Phys. Plasmas* **2017**, *24*, 073502.
[46] Y. Ohko, Y. Nakamura, A. Fukuda, S. Matsuzawa, K. Takeuchi, *J. Phys. Chem. C* **2008**, *112*, 10502.
[47] T. Luttrell, S. Halpegamage, J. Tao, A. Kramer, E. Sutter, M. Batzill, *Sci. Rep.* **2014**, *4*, 4043.
[48] T. E. Weirich, M. Winterer, S. Seifried, H. Hahn, H. Fuess, *Ultramicroscopy* **2000**, *81*, 263.
[49] T. Mashimo, R. Bagum, Y. Ogata, M. Tokuda, M. Okube, K. Sugiyama, Y. Kinemuchi, H. Isobe, A. Yoshiasa, *Cryst. Growth Des.* **2017**, *17*, 1460.
[50] P. Lamichhane, B. Ghimire, S. Mumtaz, R. Paneru, S. H. Ki, E. H. Choi, *J. Phys. D* **2019**, *52*, 265206.
[51] N. Pourali, K. Lai, J. Gregory, Y. Gong, V. Hessel, E. V. Rebrov, *Plasma Processes Polym.* **2023**, *20*, 2200086.
[52] J. Liang, Y. Jiao, M. Jaroniec, S. Z. Qiao, *Angew. Chem.* **2012**, *124*, 11664.
[53] J. Goodings, D. Bohme, C.-W. Ng, *Combust. Flame* **1979**, *36*, 45.
[54] A. Rahman, A. Yalin, V. Surla, O. Stan, K. Hoshimiya, Z. Yu, E. Littlefield, G. Collins, *Plasma Sources Sci. Technol.* **2004**, *13*, 537.
[55] B. Hrycak, M. Jasiński, J. Mizeraczyk, *J. Phys. Conf. Ser.* **2012**, *406*, 012037.
[56] S. I. Hosseini, S. Mohsenimehr, J. Hadian, M. Ghorbanpour, B. Shokri, *Phys. Plasmas* **2018**, *25*, 013525.
[57] P. Bruggeman, D. Schram, M. Á. González, R. Rego, M. G. Kong, C. Leys, *Plasma Sources Sci. Technol.* **2009**, *18*, 025017.
[58] M. Camero, F. J. Gordillo-Vázquez, J. Ortiz, C. Gómez-Aleixandre, *Plasma Sources Sci. Technol.* **2003**, *13*, 121.
[59] D. Xiao, C. Cheng, J. Shen, Y. Lan, H. Xie, X. Shu, Y. Meng, J. Li, P. K. Chu, *J. Appl. Phys.* **2014**, *115*, 033303.

[60] J. F. Kolb, A.-A. H. Mohamed, R. O. Price, R. J. Swanson, A. Bowman, R. L. Chiavarini, M. Stacey, K. Schoenbach, *Appl. Phys. Lett.* **2008**, *92*, 241501.
[61] G.-D. Stancu, F. Kaddouri, D. Lacoste, C. Laux, *J. Phys. D* **2010**, *43*, 124002.
[62] P. Dimitrakellis, M. Giannoglou, A. Zeniou, E. Gogolides, G. Katsaros, *MethodsX* **2021**, *8*, 101177.
[63] H. Hartl, Y. Guo, K. Ostrikov, Y. Xian, J. Zheng, X. Li, K. E. Fairfull-Smith, J. MacLeod, *RSC Adv.* **2019**, *9*, 2848.
[64] P. Attri, F. Tochikubo, J. H. Park, E. H. Choi, K. Koga, M. Shiratani, *Sci. Rep.* **2018**, *8*, 2926.
[65] C.-C. Hsu, Y.-J. Yang, *IEEE Trans. Plasma Sci.* **2010**, *38*, 496.
[66] E. Janić Hajnal, M. Vukić, L. Pezo, D. Orčić, N. Puač, N. Škoro, A. Milidrag, D. Šoronja Simović, *Toxin Rev.* **2019**, *11*, 704.
[67] Z. Fan, H. Yan, Y. Wang, Y. Liu, H. Guo, C. Ren, *Phys. Plasmas* **2018**, *25*.
[68] D. Popović, V. Milosavljević, S. Daniels, *J. Appl. Phys.* **2007**, *102*.
[69] P. Thana, A. Wijaikhum, P. Poramapijitwat, C. Kuensaen, J. Meerak, A. Ngamjarurojana, S. Sarapirom, D. Boonyawan, *Heliyon* **2019**, *5*.
[70] P. Attri, E. H. Choi, *PLoS One* **2013**, *8*, e75096.
[71] N. Pourali, P. Lamichhane, V. Hessel, E. V. Rebrov, *Plasma Processes and Polymers* **2023**, page e2300007.
[72] C. Ang, *Acta Metall.* **1953**, *1*, 123.
[73] H. M. Joh, J. Y. Choi, S. J. Kim, T. Chung, T.-H. Kang, *Sci. Rep.* **2014**, *4*, 1.
[74] J. F. da Silveira Petruci, P. R. Fortes, V. Kokoric, A. Wilk, I. M. Raimundo, A. A. Cardoso, B. Mizaikoff, *Sci. Rep.* **2013**, *3*, 1.
[75] M. Pavlovich, T. Ono, C. Galleher, B. Curtis, D. Clark, Z. Machala, D. Graves, *J. Phys. D* **2014**, *47*, 505202.
[76] J. M. Dorhout, A. S. Anderson, E. Batista, R. K. Carlson, R. P. Currier, R. K. Martinez, S. M. Clegg, M. P. Wilkerson, K. Nowak-Lovato, *J. Mol. Spectrosc.* **2020**, *372*, 111334.
[77] J. Osorio-Tejada, N. N. Tran, V. Hessel, *Sci. Total Environ.* **2022**, *826*, 154162.
[78] J. Osorio-Tejada, K. van't Veer, N. V. D. Long, N. N. Tran, L. Fulcheri, B. S. Patil, A. Bogaerts, V. Hessel, *Energy Convers. Manage.* **2022**, *269*, 116095.
[79] P. Liu, B. Chen, C. Liang, W. Yao, Y. Cui, S. Hu, P. Zou, H. Zhang, H. J. Fan, C. Yang, *Adv. Mater.* **2021**, *33*, 2007377.
[80] G. J. Schulz, *Phys. Rev.* **1962**, *125*, 229.
[81] T. Haruyama, T. Namise, N. Shimoshimizu, S. Uemura, Y. Takatsuji, M. Hino, R. Yamasaki, T. Kamachi, M. Kohno, *Green Chem.* **2016**, *18*, 4536.
[82] Y. Kim, S. M. Stange, L. A. Rosocha, V. W. Ferreri, *J. Adv. Oxid. Technol.* **2005**, *8*, 188.
[83] P. Lamichhane, N. Pourali, L. Scott, N. N. Tran, L. Lin, M. E. Gelonch, E. V. Rebrov, V. Hessel, *Renewable Sustainable Energy Rev.* **2024**, *189*, 114044.
[84] M. Moravej, X. Yang, M. Barankin, J. Penelon, S. Babayan, R. Hicks, *Plasma Sources Sci. Technol.* **2006**, *15*, 204.
[85] A. Gómez-Ramírez, J. Cotrino, R. Lambert, A. González-Elipe, *Plasma Sources Sci. Technol.* **2015**, *24*, 065011.
[86] T. Sakakura, Y. Takatsuji, M. Morimoto, T. Haruyama, *Electrochemistry* **2020**, *88*, 190.
[87] L. R. Winter, J. G. Chen, *Joule* **2021**, *5*, 300.
[88] P. Attri, Y. H. Kim, D. H. Park, J. H. Park, Y. J. Hong, H. S. Uhm, K.-N. Kim, A. Fridman, E. H. Choi, *Sci. Rep.* **2015**, *5*, 1.
[89] H. S. Uhm, S. H. Ki, K. Y. Baik, E. H. Choi, *Sci. Rep.* **2018**, *8*, 9318.
[90] K. Gazeli, P. Svarnas, B. Held, L. Marlin, F. Clement, *J. Appl. Phys.* **2015**, *117*, 093302.
[91] E. Vervloessem, Y. Gorbanev, A. Nikiforov, N. De Geyter, A. Bogaerts, *Green Chem.* **2022**, *24*, 916.
[92] M. Scapinello, E. Delikonstantis, G. D. Stefanidis, *Chem. Eng. Process.* **2017**, *117*, 120.
[93] F. Van Steenweghen, L. Hollevoet, J. A. Martens, *Green Chem.* **2024**, *26*, 2534.
[94] S. C. Capp, D. A. Sawtell, C. E. Banks, P. J. Kelly, Z. Abd-Allah, *J. Environ. Chem. Eng.* **2021**, *9*, 106046.
[95] P. Li, M. Guo, Q. Wang, Z. Li, C. Wang, N. Chen, C.-C. Wang, C. Wan, S. Chen, *Appl. Catal. B* **2019**, *259*, 118107.
[96] Y. Wu, H. Ji, Q. Liu, Z. Sun, P. Li, P. Ding, M. Guo, X. Yi, W. Xu, C.-C. Wang, et al., *J. Hazard. Mater.* **2022**, *424*, 127563.
[97] P. Ding, H. Ji, P. Li, Q. Liu, Y. Wu, M. Guo, Z. Zhou, S. Gao, W. Xu, W. Liu, et al., *Appl. Catal. B* **2022**, *300*, 120633.
[98] A. K. Sibhatu, G. K. Weldegebrieal, S. Sagadevan, N. N. Tran, V. Hessel, *Chemosphere* **2022**, page 134623.
[99] R. Sharma, P. P. Das, M. Misra, V. Mahajan, J. P. Bock, S. Trigwell, A. S. Biris, M. K. Mazumder, *Nanotechnology* **2009**, *20*, 075704.
[100] C. Zhang, Y. Huang, B. Zhao, Y. Yu, Y. Yu, B. Zhang, *J. Catal.* **2022**, *409*, 70.
[101] S.-J. Yuan, J.-J. Chen, Z.-Q. Lin, W.-W. Li, G.-P. Sheng, H.-Q. Yu, *Nat. Commun.* **2013**, *4*, 2249.
[102] J. Nowotny, T. Bak, M. Nowotny, L. Sheppard, *J. Phys. Chem. B* **2006**, *110*, 18492.
[103] M. Janczarek, E. Kowalska, *Catalysts* **2017**, *7*, 317.
[104] K. Hu, E. Lei, D. Zhao, Y. Li, W. Zhao, H. Rong, *CrystEngComm* **2020**, *22*, 1086.
[105] J. Wang, W. Lin, Y. Ran, J. Cui, L. Wang, X. Yu, Y. Zhang, *J. Phys. Chem. C* **2019**, *124*, 1253.
[106] R. Huang, X. Li, W. Gao, X. Zhang, S. Liang, M. Luo, *RSC Adv.* **2021**, *11*, 14844.
[107] G. Zhang, X. Yang, C. He, P. Zhang, H. Mi, *J. Mater. Chem. A* **2020**, *8*, 334.

Manuscript received: March 4, 2024